# Nanofiber-Textured Organic Semiconductor Films for Field-Effect Ammonia Sensors

**YAO TANG** [1], **QING MA**[2], **JIE LU**[3], **XINGYU JIANG**[3], **LIZHEN HUANG**[3], **LIFENG CHI**[3] **(Member, IEEE),**
**LITAO SUN** [1,2], **AND BINGHAO WANG** [1,2]

[1]School of Microelectronics, Southeast University, Nanjing, Jiangsu 211189, China
[2]School of Electronic Science and Engineering, Southeast University, Nanjing, Jiangsu 211189, China
[3]Institute of Functional Nano & Soft Materials (FUNSOM), Soochow University, Suzhou, Jiangsu 215006, China

CORRESPONDING AUTHORS: LIFENG CHI; LITAO SUN; BINGHAO WANG (e-mail: chilf@suda.edu.cn; slt@seu.edu.cn; binghaowang@seu.edu.cn).

**ABSTRACT** Field-effect gas sensors, integrating the gas sensor and amplification transistor, exhibit excellent sensory performance. Here we report organic thin-film transistors (OTFTs) with nanofiber-textured semiconductor films that exhibit superior ammonia response compared to conventional OTFTs with uniform/flat semiconductor films. The introduce of insulating polymer additives (IPAs) facilitates the formation of semiconducting nanofiber during coating. The effects of IPAs, organic semiconductor/IPA blend ratios and solvents on OTFT-based sensory performance are studied. The results show that the use of SU8 as IPA and chloroform as solvent form intertwined semiconductor nanofibers (∼50 nm in diameter) at the bottom. The resulting OTFTs exhibit extraordinarily high sensitivities to ammonia, which reach 13676%/ppm (current) and 457%/ppm (turn-on voltage), respectively. Finite element analysis is conducted to simulate the adsorption/desorption processes of gas molecules and the effect of specific surface area on sensory performance.

**INDEX TERMS** Organic thin-film transistors, gas sensors, semiconducting nanofibers, finite element analysis.

## I. INTRODUCTION

Owing to the weak-signal amplification characteristics, organic thin-film transistors (OTFTs) outperform two-terminal resistors in high-sensitivity sensors used for light, pressure, chemical, and biochemical detections, etc. [1], [2], [3], [4]. Typically, OTFTs are built on uniform organic semiconductor (OSC) films to yield good device performance and stability, nevertheless, the continuous OSC film influences interactions with analytes when using for sensors, thus the analytes cannot effective diffuse into the charge accumulation region [5].

In the past decade, several strategies have been proposed to facilitate the exposure of the charge transport layer to analytes, such as, air-dielectric structure [6], ultrathin (<5 nm-thick) OSC film [7], [8], porous OSC film [9]. For example, Qiu's and Marks's group reported the formation of porous OSC films by phase separation and breath-figure method, respectively [9], [10], [11], [12]. Such films provide conductive

pathways at the OSC/dielectric interfaces, while the presence of nanopores facilitate the diffusion of analytes throughout the channels [13], [14]. Thus, the resulting OTFTs exhibit significantly enhanced ammonia sensitivity and fast response time [15], [16]. However, detailed investigations of porous OTFTs-based gas sensors with different blend ratios, insulating polymer additives (IPAs), and the solvents used are missing. Also, theoretic simulation may help the understanding the adsorption and desorption processes of gases [17], [18], [19], [20], which have never been reported for these porous OSC films [21], [22].

In previous work, we verified the vertical phase separation between poly[25-bis (2-octyldodecyl) -36-diketopyrrolopyrrole-alt-5,5'- (25-di (thien-2-yl) thieno[32-b] thiophene)] (abbreviated as DPP) and insulating polymer (SU-8 2000.5), where the OSC was formed in the underlying layer [23]. Here, we achieve DPP films with
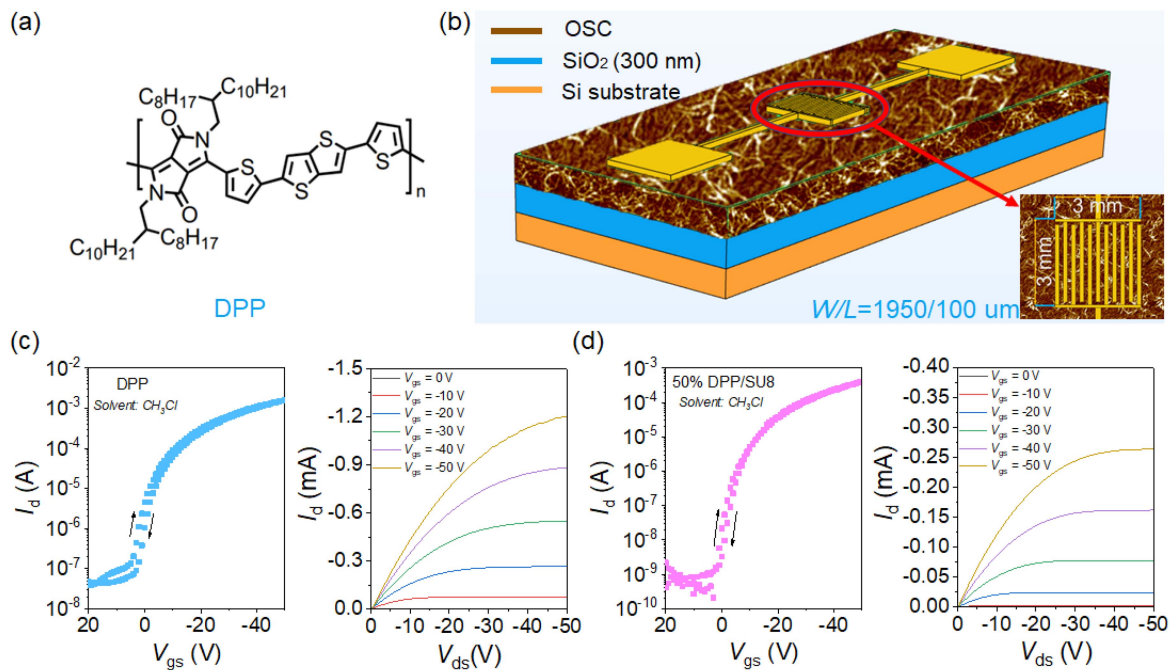
**FIGURE 1.** (a) Chemical structure of DPP organic semiconductor. (b) Schematic structure of OTFT devices. (c) Transfer and output curves of DPP OTFT processed from chloroform. (d) Transfer and output curves of 50%DPP/SU8 OTFT processed from chloroform.

nanofiber-textures by selectively removing the upper IPAs. OTFTs based on such DPP films are more sensitive when exposure to ammonia, with concentrations vary from 1 ppm to 23 ppm. The effects of blend ratio, solvent and IPA on the morphology, OTFTs' and gas sensory performance are systematically studied. Moreover, finite element simulation was conducted to simulate the adsorption/desorption processes of gas molecule and the roles of specific surface area.

## II. EXPERIMENTAL SECTIONS
### A. MATERIALS
Poly[25-bis (2-octyldodecyl) -36-diketopyrrolopyrrole-alt-5,5'- (25-di (thien-2-yl) thieno[32-b] thiophene)] (abbreviated as DPP) was purchased from 1-Material Inc. Its chemical structure is given in Fig. 1(a). Trichloro(octyl)silane (OTS), polymethyl methacrylate (PMMA, average $M_w$ ~120 kg $mol^{-1}$), anhydrous chloroform and 1,2-dichlorobenzene (o-DCB) were purchased from Sigma-Aldrich. SU-8 2000.5 photoresist and SU8 developer were purchased from Kayaku Advanced Materials, Inc. The silicon substrates with 300 nm-thick $SiO_2$ were purchased from Suzhou Resemi Co., Ltd.

### B. PREPARATION OF PRECURSOR SOLUTIONS AND SUBSTRATES
Exactly 8 mg of DPP and 8 mg of PMMA were separately dissolved in 2 mL of chloroform or o-DCB for form 4 mg $mL^{-1}$ solutions. Next, 50 $\mu$L SU-8 2000.5 photoresist was diluted with 1.89 mL of chloroform or o-DCB to form 4 mg $mL^{-1}$ solutions. All the solutions were stirred for at least 2 hour at 45 °C in a glovebox.

With regard to the preparation of OTS-treated $SiO_2$/Si substrates, the clean $SiO_2$/Si substrates were first treated with an $O_2$ plasma for 5 min. Then, 20 $\mu$L of OTS solution was drop on the center of petri dish, where have $SiO_2$/Si substrates around. After that, the petri dish was put in a vacuum oven and heat it at 130 °C for 90 minutes. Finally, the oven is naturally cooled down to room temperature.

### C. FABRICATION OF DPP, DPP/SU8 AND DPP/PMMA OTFTS
The DPP solution is separately blend with PMMA and SU8 solutions with a volume ratio of 1:2, 1:1, and 2:1, for fabricating the 33%, 50%, and 66% DPP/SU8 and DPP/PMMA blends. Identical solvents were used for each blend. Then the mixed solutions were kept stirring at 45 °C for 1 h. After that, the mixed solution was spin-coated on OTS-treated $SiO_2$/Si substrates at 2000 rpm for 30 s in the glove box. After prebaking at 95 °C for 1 min, the films were sequentially rinsed in SU8 developer and isopropyl alcohol for 10 s to selectively remove upper SU8 and PMMA, followed by annealing at 150 °C for 30 min under ambient. Finally, gold source/drain electrode was deposited through a metal mask to form bottom-gate top-contact OTFTs with a channel size of $W/L = 19500/100$ $\mu$m (Fig. 1(b)).

### D. FILM AND DEVICE CHARACTERIZATION
Film morphologies were measured with a Bruker Dimensional Icon AFM system in the tapping mode. The electrical measurements for the OTFTs were performed under ambient condition using a Keithley 4200-SCS semiconductor
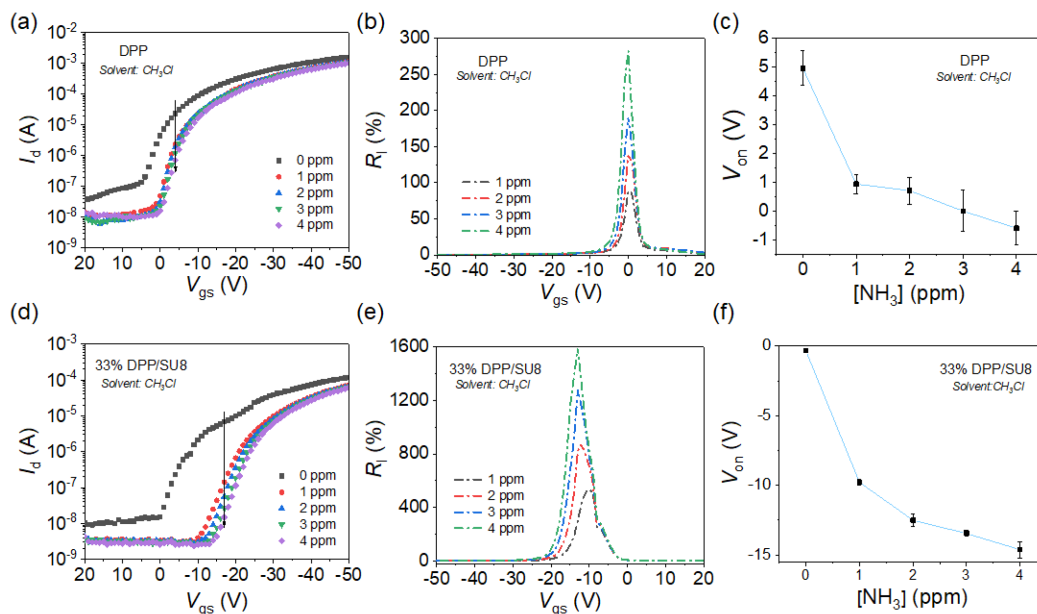
**FIGURE 2.** (a) Transfer curves (b) Current responsivity ($R_I$)-$V_{gs}$ plots and (c) turn-on voltages ($V_{on}$) of chloroform-processed DPP OTFTs exposed to different $NH_3$ concentrations. (c) Transfer curves (d) $R_I$-$V_{gs}$ plots and (e) $V_{on}$ of chloroform-processed 33%DPP/SU8 OTFTs exposed to different $NH_3$ concentrations.

parameter analyzer. Electrical parameters were extracted using standard MOSFET equations and the carrier mobility ($\mu$) was evaluated in the saturation region. The areal capacitance for 300 nm $SiO_2$/Si is 10.5 nF $cm^{-2}$ here.

For gas sensor test, the devices were measured under $NH_3/N_2$ gas. 1-23 ppm $NH_3$ was obtained by diluting 100 ppm $NH_3/N_2$ (Linde Industrial Gases, Suzhou) with pure $N_2$ with the aid of an automatic gas distribution system (Beijing Kingsun Electronics Co., Ltd, China). The OTFT devices underwent 10 minutes of $N_2$ flushing before exposed to $NH_3/N_2$. The purging time of $NH_3/N_2$ and pure $N_2$ is set as 240 s and 600 s, respectively.

## III. EXPERIMENT RESULTS AND DISCUSSION

First, we tested and compared the TFT-based ammonia sensory performance for DPP and 50% DPP/SU8 TFTs with the OSC layers were processed from chloroform. Note that the upper surface of 50% DPP/SU8 was rinsed by SU8 developer to form DPP nanofiber texture. This rinsing step is applicable for all the following OTFT devices unless otherwise noted. As shown in the transfer and output plots of Fig. 1(c) and (d), the DPP-based OTFTs exhibit typical p-type behavior and their electrical parameters are summarized in Table S1. The average $\mu$ and threshold voltage ($V_T$) for the DPP devices are 0.48 $cm^2$ $V^{-1}$ $s^{-1}$ and −0.41 V, respectively, while the mobilities ($V_T$) of the 50% DPP/SU8 is 0.23 $cm^2$ $V^{-1}$ $s^{-1}$ (−1.52 V), indicating a certain degree of performance degradation during blending and rinsing.

Up on exposure to ammonia, the on-current ($I_{on}$, drain current measured at $V_{ds} = V_{gs} = −50$ V) of DPP TFTs decrease from $1.59 \times 10^{-3}$ A to $1.01 \times 10^{-3}$ A as the concentration of

$NH_3$ increases from 0 to 4 ppm (Fig. 2(a)). Current responsivity ($R_I$) is defined as (1), where, $R_{gas}$ refers to the resistance of the device at a specific analyte concentration and $R_0$ refers to the original resistance. [24], [25] According to Ohm's law, the (2) can be obtained where $I_0$ and $I_{gas}$ refer to the device current at initial status and exposed status with specific analyte concentration, respectively.

$$R_I (\%) = \frac{R_{gas} - R_0}{R_0} \times 100\% \qquad (1)$$

$$R_I (\%) = \frac{I_{gas} - I_0}{I_{gas}} \times 100\% \qquad (2)$$

The $R_I\%$ of DPP OTFTs to ammonia is the largest when the $V_{gs}$ is around 0 V, and it reaches to 28200% at [$NH_3$] = 4 ppm, much higher than that ($R_I\% = 50\%$) of $V_{gs} = −50$ V. Meanwhile, a shift of the turn-on voltage ($V_{on}$) toward negative values ($\Delta V_{on} = −5.6$ V) is observed (Fig. 2(b)). Regarding 33%DPP/SU8 OTFTs, significant higher response is observed with largest $\Delta V_{on}$ and $R_I\%$ reach to −14.3 V and 160000%, respectively (Fig. 2(e) and (f)).

Then we investigate the effect of solvent on the OTFT-based sensory performance. Chloroform and *o*-DCB were chosen as they have different boiling points (61.2 °C *Vs* 179 °C), which would greatly affect the evaporating time during spin-coating. Thus, the morphology and microstructure of OSC films and device performance processed from different solvents could vary dramatically. Fig. 3 compares the 50%DPP/SU8 OTFTs-based sensory performance, which were processed from chloroform and *o*-DCB, respectively. The $I_{on}$ and average $\mu$ of chloroform-derived 50%DPP/SU8 OTFTs are $4.04 \times 10^{-4}$ A and 0.23 $cm^2V^{-1}s^{-1}$, respectively,
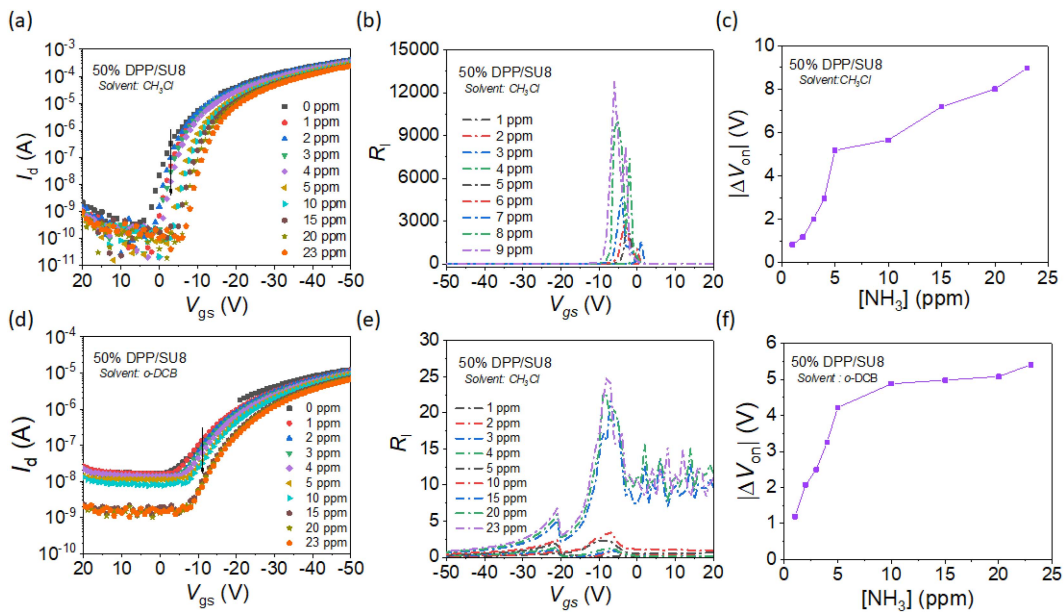
**FIGURE 3.** (a) Transfer curves (b) $R_I$-$V_{gs}$ plots and (c) $V_{on}$ shift of chloroform-processed 50%DPP/SU8 OTFTs exposed to different NH$_3$ concentrations. (d) Transfer curves (e) $R_I$-$V_{gs}$ plots and (f) $V_{on}$ shift of *o*-DCB-processed 50%DPP/SU8 OTFTs exposed to different NH$_3$ concentrations.
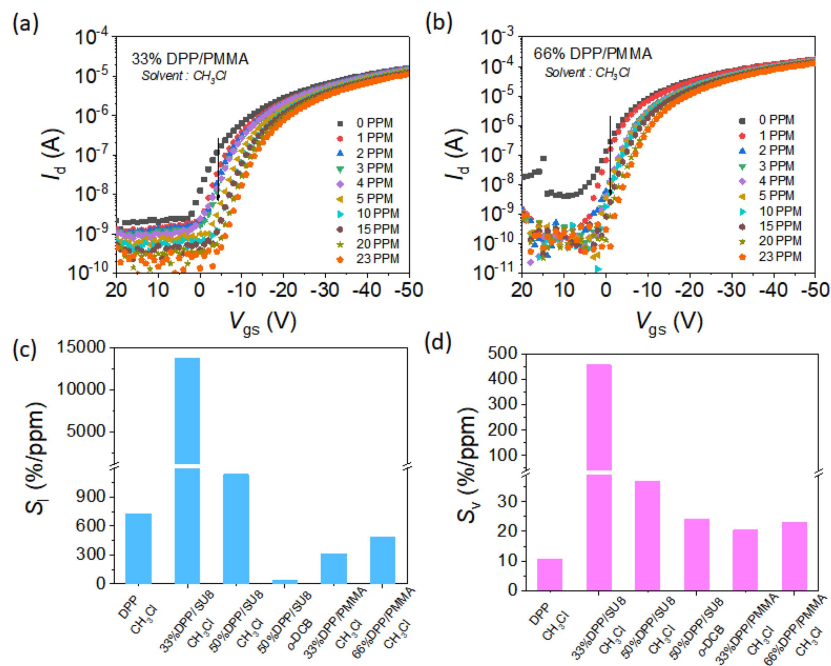


**FIGURE 4.** Transfer curves of chloroform-processed (a) 33%DPP/PMMA OTFTs and (b) 66%DPP/PMMA OTFTs exposed to different NH$_3$ concentrations. (c) Current sensitivity ($S_I$%) and (d) $V_{on}$ sensitivity ($S_V$%) of indicated OTFTs, the calculation of $S_I$% is based on the values through which the arrows pass in the corresponding figures.

which are much higher than those ($1.2 \times 10^{-5}$A and 0.005 cm$^2$V$^{-1}$s$^{-1}$), of *o*-DCB-derived 50%DPP/SU8 OTFTs. Their gas sensory performance is also different. The maximum $R_I$% and $|\Delta V_{on}|$ for *o*-DCB-derived 50%DPP/SU8 OTFTs when exposed to 23 ppm NH$_3$ are 2400% and 5.41 V, respectively , while the improved $R$% (= 1282500%) and $\Delta V_{on}$ (= 8.96 V) are achieved for chloroform-derived 50%DPP/SU8 OTFTs.

The types of IPAs also affect the TFT mobility and sensory performance. When chloroform is used, but SU8 is replaced by PMMA, much lower average $\mu$ are obtained, which are 0.005 cm$^2$ V$^{-1}$ s$^{-1}$ and 0.05 cm$^2$ V$^{-1}$ s$^{-1}$ for 33% DPP/PMMA and 66%DPP/PMMA OTFTs (Fig. 4(a) and (b)). Also, their electrical responses when exposed to NH$_3$ are much weaker with largest $R_I$%
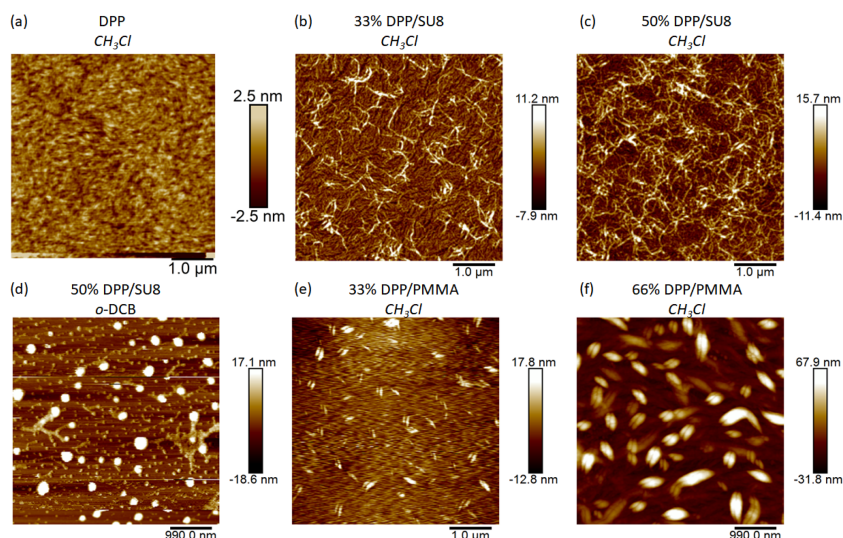
**FIGURE 5.** (a)–(f) AFM images of indicated semiconductor films. The top layers of blended films were rinsed away by SU8 developer before AFM measurement.

and $|\Delta V_{on}|$ for 33% DPP/PMMA OTFTs are 49400% and 4.41V, respectively (Fig. S1). Fig. 4(c) and (d) summarize the current sensitivity ($S_I\% = R_I\%$/ppm) and $V_{on}$ sensitivity ($S_V\% = \Delta V_{on}/V_{on@0ppm}\%$/ppm) for representative DPP-based OTFTs. The $S_I\%$ and $S_V\%$ are the slopes of the linear relationships of $R_I\%$ $vs$ $NH_3$ concentration and $\Delta V_{on}/V_{on@0ppm}\%$ $vs$ $NH_3$ concentration. Similar trends are observed that $CH_3Cl$-derived DPP/SU8 OTFTs exhibit extraordinarily high $S_I\%$ and $S_V\%$, which reach 13676%/ppm and 457%/ppm, respectively. The improvements of the sensory performance of $o$-DCB-derived OTFTs and PMMA-processed DPP/SU8 OTFTs are limited. Seen from their atomic force microscope (AFM) images (Fig. 5), the DPP film processed from $CH_3Cl$ has a thickness of $\sim$120 nm and exhibits very smooth surface with a root-mean-square (rms) roughness of 0.6 nm. The $CH_3Cl$-derived 33%DPP/SU8 films has a thickness of only $\sim$8.0 nm after removing upper layer (Fig. S6). Its surface exhibits nanofiber morphologies with a fiber diameter $\sim$50 nm. Such fiber network structure with high surface specific ratio is very beneficial to interact with the ammonia. The AFM images of DPP/PMMA film also exhibit fiber texture but with much larger diameter ($\sim$300 nm).

Real-time responses (reciprocal of the current) were next measured for devices biased at $V_{ds} = 1$ V, responding to the dynamic switching to ammonia exposures (5, 10, 15, 20 and 25 ppm, Fig. 6). The resistance increases dramatically with increasing ammonia concentration, especially for nanofiber-textured DPP/SU8 OTFTs. When the devices exposed to the same $NH_3$ concentration, the responsivity decreases as the increasing DPP concentration. For example, the resistance of 33% DPP/SU8 OTFTs dramatically increases from 1.4 G$\Omega$ (0 ppm) to 124.5 G$\Omega$ (15 ppm), while the resistance of 66% DPP/SU8 OTFTs slightly increases from 0.17 G$\Omega$ (0 ppm) to 9.4 G$\Omega$ (15 ppm). Also, rapid response and recovery time

were observed, which are 118 s and 188 s for 33% DPP/SU8 OTFTs, respectively, which are much faster than those (203 s and 507 s) of DPP OTFTs.

## IV. FINITE ELEMENT SIMULATION OF OTFT-BASED GAS SENSOR

To further understanding the dynamic adsorption and desorption of gas molecules on nanofiber texture, finite element analysis (FEA) was carried out. A three-dimensional model is established to mimic actual test setup (Fig. 7(a)).

The model device consists of 1-mm thick silicon substrate, 300 nm-thick $SiO_2$, 20 nm-thick OSC layer and 40 nm-thick gold electrodes. The detailed geometric and physical/chemical parameters of the model, such as height, radius, adsorption/desorption rates, are given in Table S3. Also, the OSC surface are divided into super fine grids to accurate simulation (Fig. S2). Compared to the dense and flat film, the nanofiber morphology greatly improves the rate of adsorption and desorption by increasing the effective contact volume with analyte molecules. Here, we introduce specific surface area (SSA) as a dimensionless parameter to explain the difference between flat and nanofibrous films [26], [27].

$$SSA = \frac{pore\ surface\ area}{total\ volume} = \frac{\sum_1^{number\ of\ pores} 4d \cdot h}{L^2 \cdot h} \quad (3)$$

$$S_r \times SSA = EV_r \quad (4)$$

Where $h$ refers to the reacting area thickness of the OSC layer, $S_r[mol \cdot m^{-2} \cdot s^{-1}]$ represents the surface reaction rate, and $EV_r$ represents effective volume reaction rate.

Before establishing the mathematical model of this paper, we make the following assumptions: 1) The heat released and absorbed during the adsorption and desorption of gas molecules is small enough to not affect the operating temperature of the entire device. 2) The thickness of the OSC layer
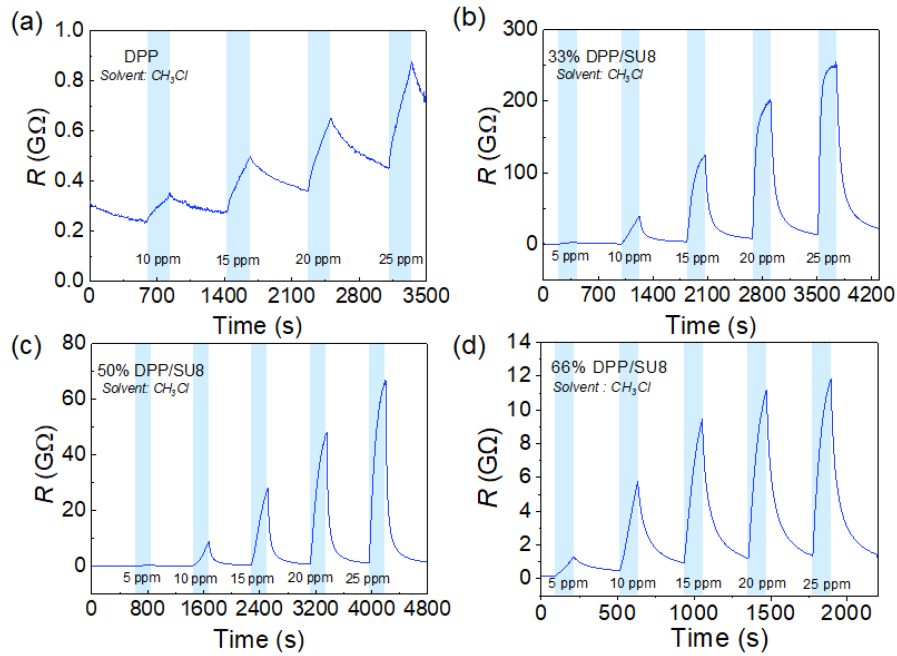
**FIGURE 6.** (a)–(d) Dynamic Real-time responses of indicated OTFTs ($V_{ds} = 1$ V) responding to dynamic switching between $NH_3$ concentrations.
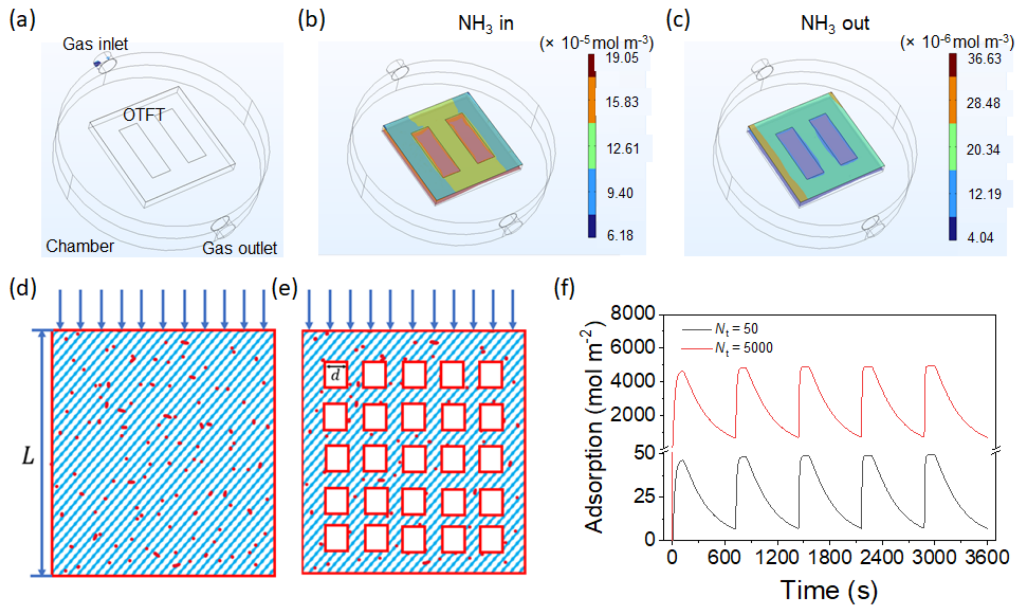


**FIGURE 7.** (a) 3D model of test chamber with OTFT inside. (b) The distributions of $NH_3$ concentration around the OTFTs during purging (b) $NH_3/N_2$ and (c) $N_2$, respectively. (d) The simulated distribution of active sites for (d) flat and (e) nanofibrous films. The nanofibrous morphology is simplified as squares with length of $d$. (f) The dynamic adsorption of $NH_3$ for OSC film with $N_t = 50$ and 5000, respectively.

is thin enough so that the distance from the gas molecules to be adsorbed to the active sites is the same, and there is no difference between these active sites. Permeability is not considered. 3) A single gas molecule can only be adsorbed on one active site. 4) Adsorption and desorption occur at the same time without any molecular interference. 5) The increased active sites originated from the nanofiber texture would not affect original active sites from the membrane surface. 6) both the flat and nanofiber-textured films are uniform that homogenization method can be used [17], [18], [19].

As the interaction between gas analyte and OTFTs can be regarded as isothermal to avoid the calculation complexity. Langmuir isotherm adsorption model was applied and the gas molecules adsorbed on the surface of the sensing layer are in a dynamic equilibrium [28], [29], [30].

$$\frac{\partial c_s}{\partial t} + \nabla \cdot (-D_s \nabla c_s) = r_{\text{ads\_NH}_3} - r_{\text{des\_NH}_3} \qquad (5)$$

Equation 5 describes the material conservation of ammonia analyte molecules on the sensing surface. $r_{\text{ads\_NH}_3}$ and

$r_{\text{ads\_NH}_3}$ represent the adsorption rate and desorption rate, respectively. $c_s$ is the total concentration of adsorbate (mol m$^{-2}$) and $D_s$ is the surface diffusion coefficient.

There are several relationships are shown in Equations (6)–(9):

$$\theta = \frac{C_s}{N_t} \qquad (6)$$

$$r_{\text{ads\_NH}_3} = k_a \cdot p_a \cdot (1 - \theta) \qquad (7)$$

$$r_{\text{des\_NH}_3} = k_r \cdot \theta \qquad (8)$$

$$p_a = \text{CRT} \qquad (9)$$

Where $\theta$ refers to the proportion of the active sites occupied by the adsorbate. $N_t$ is total surface concentration of active sites (mol m$^{-2}$). $p_a$ refers to the gas pressure. $C$ is the environmental gas analyte concentration (mol m$^{-3}$). $R$ and $T$ refer to gas constants ($= 8.314$ J·mol$^{-1}$·K$^{-1}$) and Kelvin temperature, respectively. $k_a$ is the adsorption constant and $k_r$ is the desorption constant.

Thus, we have the following Equations (10)–(12):

$$r_{\text{des\_NH}_3} = k_{\text{des\_NH}_3} \cdot c_s \qquad (10)$$

$$r_{\text{ads\_NH}_3} = k_{\text{ads\_NH}_3} C \left( N_t - c_s \right) \qquad (11)$$

$$\frac{\partial c_s}{\partial t}\Big|_{t=0} = max\ r_{\text{ads\_NH}_3} \qquad (12)$$

Equation (12) can be used to calculate the initial rate value of gas adsorption, which typically exhibit strong and rapid gas response.

First, we simulate the dynamic change of ammonia concentration, which are identical to the actual test environment (Fig. 7(a) and Fig. S3). From the isosurface of NH$_3$ concentration around the OTFTs (Fig. 7(b) and (c)), we observe an increased NH$_3$ concentration around the channel when NH$_3$ is introduced. From the experimental results, the resistance of OTFTs increases significantly upon expose to ammonia, then the increasing rate slow down until reach a plateau. In such process, the competition between gas adsorption and desorption plays a major role in electrical response [22], [31]. By intercepting gas response of the devices' geometric center point using the above equations (Fig. S4), we obtained the Fig. 7(f), showing that different $N_t$ do greatly affect the gas response of the simulated device. As $N_t$ is increasing, the initial absorption rate is faster and the the final equilibrium height is higher. The gas absorption at the devices' center line is given in Fig. S5.

## VI. CONCLUSION

We demonstrate a strategy for forming nanofiber texture of OSCs and its advantages in OTFT-based ammonia sensor. Through detailed studies on the effects of IPAs, solvent and blend ratio, we found the use of SU8 and chloroform yields ideal intertwined nanofiber ($\sim$50 nm) morphology and good superior OTFT and sensory performance. To reflect the advantages of OTFT devices in gas sensor, two quantization parameters (current sensitivity and $V_{\text{on}}$ sensitivity) were introduced and compared simultaneously. The FEA simulation also verified the increased active sites are beneficial for faster response and higher sensitivity.

## REFERENCES

[1] J. Milvich et al., "Flexible low-voltage organic phototransistors based on air-stable dinaphtho[2,3-b:2′,3′-f]thieno[3,2-b]thiophene (DNTT)," *Org. Electron.*, vol. 20, pp. 63–68, 2015, doi: 10.1016/j.orgel.2015.02.007.

[2] G. D. Tabi, J. S. Kim, B. Nketia-Yawson, D. H. Kim, and Y.-Y. Noh, "High-capacitance polyurethane ionogels for low-voltage operated organic transistors and pressure sensors," *J. Materials Chem. C*, vol. 8, no. 47, pp. 17107–17113, 2020, doi: 10.1039/d0tc02364g.

[3] P. Lin and F. Yan, "Organic thin-film transistors for chemical and biological sensing," *Adv. Mater.*, vol. 24, no. 1, pp. 34–51, Jan. 3, 2012, doi: 10.1002/adma.201103334.

[4] N. Wang, A. Yang, Y. Fu, Y. Li, and F. Yan, "Functionalized organic thin film transistors for biosensing," *Acc. Chem. Res.*, vol. 52, no. 2, pp. 277–287, Feb. 2019, doi: 10.1021/acs.accounts.8b00448.

[5] C. Zhang, P. Chen, and W. Hu, "Organic field-effect transistor-based gas sensors," *Chem. Soc. Rev.*, vol. 44, no. 8, pp. 2087–2107, Apr. 2015, doi: 10.1039/c4cs00326h.

[6] T. Shaymurat, Q. Tang, Y. Tong, L. Dong, and Y. Liu, "Gas dielectric transistor of CuPc single crystalline nanowire for SO$_2$ detection down to sub-ppm levels at room temperature," *Adv. Mater.*, vol. 25, no. 16, pp. 2269–2273, Apr. 2013, doi: 10.1002/adma.201204509.

[7] L. Li et al., "High performance field-effect ammonia sensors based on a structured ultrathin organic semiconductor film," *Adv. Mater.*, vol. 25, no. 25, pp. 3419–3425, Jul. 2013, doi: 10.1002/adma.201301138.

[8] M. Mirza, J. Wang, L. Wang, J. He, and C. Jiang, "Response enhancement mechanism of NO$_2$ gas sensing in ultrathin pentacene field-effect transistors," *Org. Electron.*, vol. 24, pp. 96–100, 2015, doi: 10.1016/j.orgel.2015.05.022.

[9] Q. Wang, S. Wu, F. Ge, G. Zhang, H. Lu, and L. Qiu, "Solution-processed microporous semiconductor films for high-performance chemical sensors," *Adv. Mater. Interfaces*, vol. 3, no. 22, 2016, Art. no. 1600518, doi: 10.1002/admi.201600518.

[10] S. Wu et al., "Organic field-effect transistors with macroporous semiconductor films as high-performance humidity sensors," *ACS Appl Mater Interfaces*, vol. 9, no. 17, pp. 14974–14982, May 2017, doi: 10.1021/acsami.7b01865.

[11] X. Zhang et al., "Breath figure-derived porous semiconducting films for organic electronics," *Sci. Adv.*, vol. 6, 2020, Art. no. eaaz1042, doi: 10.1126/sciadv.aaz1042.

[12] H. Chen, Q. Hu, L. Qiu, and X. Wang, "Solution-Processed ultrathin semiconductor films for high-performance ammonia sensors," *Adv. Mater. Interfaces*, vol. 8, no. 20, 2021, Art. no. 2100493, doi: 10.1002/admi.202100493.

[13] N. D. Hoa, N. V. Duy, S. A. El-Safty, and N. V. Hieu, "Meso-/Nanoporous semiconducting metal oxides for gas sensor applications," *J. Nanomater.*, vol. 2015, pp. 1–14, 2015, doi: 10.1155/2015/972025.

[14] X. Zhuang, S. Han, B. Huai, W. Shi, and Y. Junsheng, "Sub-ppm and high response organic thin-film transistor NO2 sensor based on nanofibrillar structured TIPS-pentacene," *Sensors Actuators B: Chem.*, vol. 279, pp. 238–244, 2019, doi: 10.1016/j.snb.2018.10.002.

[15] S. Han, X. Zhuang, W. Shi, X. Yang, L. Li, and J. Yu, "Poly(3-hexylthiophene)/polystyrene (P3HT/PS) blends based organic field-effect transistor ammonia gas sensor," *Sensors Actuators B: Chem.*, vol. 225, pp. 10–15, 2016, doi: 10.1016/j.snb.2015.11.005.

[16] M. Babaei and N. Alizadeh, "Methanol selective gas sensor based on nano-structured conducting polypyrrole prepared by electrochemically on interdigital electrodes for biodiesel analysis," *Sensors Actuators B: Chem.*, vol. 183, pp. 617–626, 2013, doi: 10.1016/j.snb.2013.04.045.

[17] M. Marvi-Mashhadi, A. Vaz-Romero, F. Sket, and J. A. Rodríguez-Martínez, "Finite element analysis to determine the role of porosity in dynamic localization and fragmentation: Application to porous microstructures obtained from additively manufactured materials," *Int. J. Plast.*, vol. 143, 2021, Art. no. 102999, doi: 10.1016/j.ijplas.2021.102999.

[18] G. Martínez-Ayuso, M. I. Friswell, S. Adhikari, H. H. Khodaparast, and H. Berger, "Homogenization of porous piezoelectric materials," *Int. J. Solids Structures*, vol. 113–114, pp. 218–229, 2017, doi: 10.1016/j.ijsolstr.2017.03.003.

[19] X. Zhuang, Q. Wang, and H. Zhu, "A 3D computational homogenization model for porous material and parameters identification," *Comput. Mater. Sci.*, vol. 96, pp. 536–548, 2015, doi: 10.1016/j.commatsci.2014.04.059.

[20] S. Pal and B. Kumar, "Mathematical analysis of organic-pass transistor using pseudo-p-OTFTs," *J. Semicond.*, vol. 41, no. 6, Jun. 2020, Art. no. 062601 doi: 10.1088/1674-4926/41/6/062601.

[21] S. Li, M. Zhang, and H. Wang, "Simulation of gas sensing mechanism of porous metal oxide semiconductor sensor based on finite element analysis," *Sci. Rep.*, vol. 11, no. 1, Aug. 2021, Art. no. 17158, doi: 10.1038/s41598-021-96591-2.

[22] F. Yaghouti Niyat and M. H. Shahrokh Abadi, "COMSOL-Based modeling and simulation of SnO2/rGO gas sensor for detection of NO2," *Sci. Rep.*, vol. 8, no. 1, Feb. 2018, Art. no. 2149, doi: 10.1038/s41598-018-20501-2.

[23] B. Wang et al., "Foundry-compatible high-resolution patterning of vertically phase-separated semiconducting films for ultraflexible organic electronics," *Nature Commun.*, vol. 12, no. 1, Aug. 2021, Art. no. 4937, doi: 10.1038/s41467-021-25059-8.

[24] W. Huang et al., "UV-Ozone interfacial modification in organic transistors for high-sensitivity NO$_2$ detection," *Adv. Mater.*, vol. 29, no. 31, Aug. 2017, Art. no. 1701706, doi: 10.1002/adma.201701706.

[25] Z. Wang, L. Huang, X. Zhu, X. Zhou, and L. Chi, "An ultrasensitive organic semiconductor NO$_2$ sensor based on crystalline TIPS-Pentacene films," *Adv. Mater.*, vol. 29, Oct. 2017, Art. no. 38, doi: 10.1002/adma.201703192.

[26] E. Detsi et al., "On the specific surface area of nanoporous materials," *Acta Materialia*, vol. 59, no. 20, pp. 7488–7497, 2011, doi: 10.1016/j.actamat.2011.08.025.

[27] E. Detsi et al., "On the specific surface area of nanoporous materials," *Acta Materialia*, vol. 59, no. 20, pp. 7488–7497, 2011, doi: 10.1016/j.actamat.2011.08.025.

[28] A. Khan, S. Perveen, Z. Shaheen, and S. Qamar, "Numerical approximation of non-linear chromatographic models considering bi-langmuir isotherm," *Thermal Sci.*, vol. 26, no. 1, pp. 77–93, 2022, doi: 10.2298/Tsci200817298k.

[29] H. Maruyama and H. Seki, "Adsorption modeling by two sites Langmuir type isotherm for adsorption of bisphenol-A and diethyl phthalate onto activated carbon in single and binary system," *Separation Sci. Technol.*, vol. 57, no. 10, pp. 1535–1542, Jul. 2022, doi: 10.1080/01496395.2021.1995426.

[30] B. Hu, Y. P. Cheng, L. Wang, K. Z. Zhang, X. X. He, and M. H. Yi, "Experimental study on influence of adsorption equilibrium time on methane adsorption isotherm and Langmuir parameter," *Adv. Powder Technol.*, vol. 32, no. 11, pp. 4110–4119, Nov. 2021, doi: 10.1016/j.apt.2021.09.015.

[31] R. Cimino, K. A. Cychosz, M. Thommes, and A. V. Neimark, "Experimental and theoretical studies of scanning adsorption–desorption isotherms," *Colloids Surfaces A: Physicochem. Eng. Aspects*, vol. 437, pp. 76–89, 2013, doi: 10.1016/j.colsurfa.2013.03.025.